IET Power Electronics

Research Article

IET Journals
The Institution of Engineering and Technology

Impact of wind conditions on thermal loading of PMSG wind turbine power converters

ISSN 1755-4535
Received on 7th October 2016
Revised 12th April 2017
Accepted on 24th May 2017
doi: 10.1049/iet-pel.2016.0802
www.ietdl.org

Christopher J. Smith[1], *Christopher J. Crabtree*[1] ✉, *Peter C. Matthews*[1]

[1]*School of Engineering and Computing Sciences, Durham University, South Road, Durham, UK*

✉ *E-mail: c.j.crabtree@durham.ac.uk*

Abstract: Power converter reliability is critical for permanent magnet synchronous generator (PMSG) wind turbines. Converter failures are linked to power module thermal loading but studies often neglect turbine dynamics, control and the impact of wind speed sampling rate on lifetime estimation. This study addresses this using a 2 MW direct-drive PMSG wind turbine model with a two-level converter, and simulating junction temperatures (T_j) using a power module thermal equivalent circuit under various synthetic wind speed conditions. These synthetic wind conditions include constant and square wave profiles representing stable and gusty wind conditions. Responses to square wave wind speeds showed that the lower the gust frequency, the higher ΔT_j becomes, demonstrating that low turbulence sites have greater thermal variation in the converter. In contrast, wind speed variations with frequencies >0.25 Hz deliver only small increases in ΔT_j. It is concluded that reasonable approximations of T_j profiles can be made with 0.25 Hz wind speed data, but that lower data rate wind measurements miss essential, damaging characteristics.

1 Introduction

To meet EU renewable energy targets for 2020 and beyond, the levelised cost of energy (LCoE) of offshore wind must be reduced to below £100/MWh [1]. Operation and maintenance (O&M) accounts for ∼30% of the LCoE [2]. A key aspect of O&M is turbine sub-system reliability. By understanding which components have the greatest impact on downtime and power production, O&M resources can be focused to minimise turbine disruption and reduce the LCoE of offshore wind.

1.1 Wind turbine power converter reliability

Numerous studies have explored the reliability of wind turbine sub-systems using operational data. Carroll *et al.* [3] examined a large dataset for offshore wind turbines with mixed turbine technology to determine the main causes of failure and concluded that power converters had a typical failure rate of ∼0.2 failures/turbine/year, much lower than the highest failure rate of > 1 failure/turbine/year for pitch systems. However, a more focused study on turbine type [4] found that the failure rate of fully-rated converters (FRC) in permanent magnet synchronous generator (PMSG) turbines was 0.593 failures/turbine/year compared with 0.106 failures/turbine/year for partially-rated converters in doubly fed induction generator turbines. This suggests that the unique operating conditions of PMSG-FRCs are causing higher failure rates. Furthermore, Spring *et al.* [5] examined large wind turbine datasets and used expert knowledge to determine the impact of component failure to turbine downtime, compiling a top 30 list of failure sources. It was concluded that power converters were the highest source of turbine downtime, with their failure modes occupying the top 15 positions. Converter reliability must, therefore, be examined with a focus on the FRC in PMSG turbines.

Of the failures outlined in [4], power module failure is the failure mode for nearly all major converter repairs. Traditionally, power module failure has been linked to power module thermal loading, where the variation of temperature in the insulated gate bipolar transistors (IGBT) and diode cases causes fatigue through expansion and contraction between package layers (Fig. 1*a*). The temperature used for reference is the virtual junction temperature, ($\Delta T_{j,IGBT}$, $\Delta T_{j,diode}$), which is a virtual representation of the chip p–n junction temperature (Fig. 1*b*).

1.2 Power converter reliability studies

This approach has been applied in a number of studies to explore the expected reliability of power converters in wind turbines [7–16]. However, these studies often have limitations. Some studies neglect the impact of wind turbine dynamics and control, so wind speed inputs are directly converted into a T_j [7–9], which will deviate significantly from the true T_j profile in the converter. The use of wind speed distributions [8, 10] and large time steps, e.g. 3-hourly [11] neglects the impact of wind speed history, which has been shown to have a large impact on the current loading, and subsequently, the thermal loading of the converter [17]. For example, the use of supervisory control and advisory data acquisition (SCADA) data may only provide a mean and maximum wind speed over a 10 min period, which may hide a large amount of variation that is causing damage to the converter.

Some studies have included both realistic wind speed profiles and drive train models [12–15]. However, only two have studied a PMSG wind turbine [14, 15], and these two studies disagree whether high-frequency wind speed events impact the thermal loading of the converter significantly. There is therefore a need for a detailed study into the impact of operating conditions on power converter reliability to help inform how the turbine should be operated in order to extend its life and reduce the LCoE.

1.3 Research contributions

These limitations mean that operational profiles and failure data may not be representative of converter operation in the field, and there is no consensus on the required wind speed data frequency for accurate thermal simulation. This paper addresses these limitations by identifying the temporal fidelity over which wind events (such as gusts) cause the highest thermal variation. The minimum wind speed sampling frequency that will still provide accurate thermal profile simulation can then be determined. The impact of modelling assumptions on the estimated T_j profiles is also explored. These results will provide guidance for future simulation and experimental studies to improve converter reliability analysis accuracy, with an aim of improving best practice in both academia and industry.

To simulate these thermal loading profiles, a drive train model (Section 2.1), power loss model (Section 2.2), thermal model (Section 2.3), and wind inputs (Section 2.4) are required. The

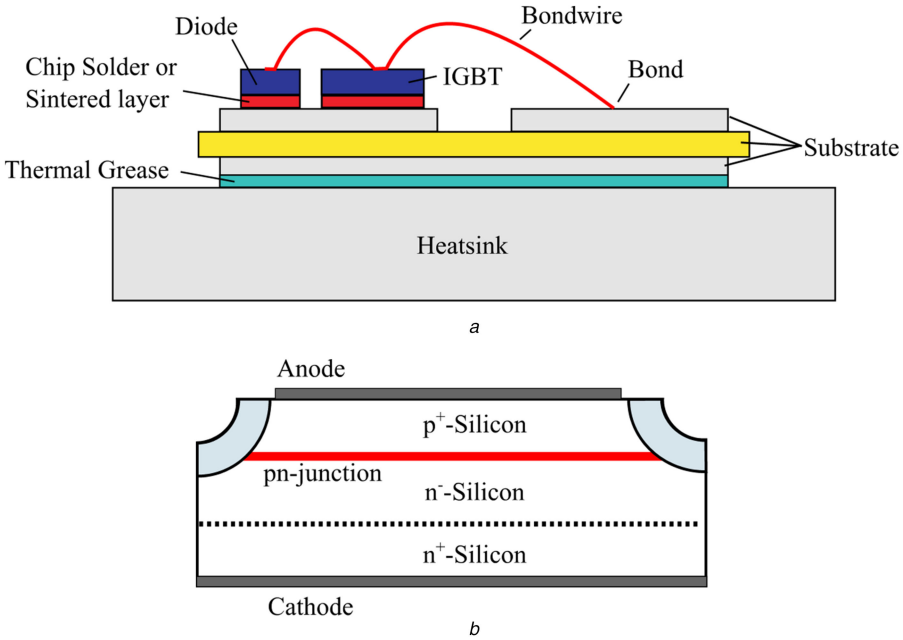

Fig. 1 *Chip layout and packaging for typical power module devices. Figures adapted from [6]*
(a) Typical IGBT power module packaging with no base plate. Areas of fatigue include the bondwire, the bondwire bonds, and the chip solder/sintered layer, ***(b)*** Internal structure of a typical p–n diode chip showing the location of the p–n junction used as the virtual reference point for $T_{j,diode}$

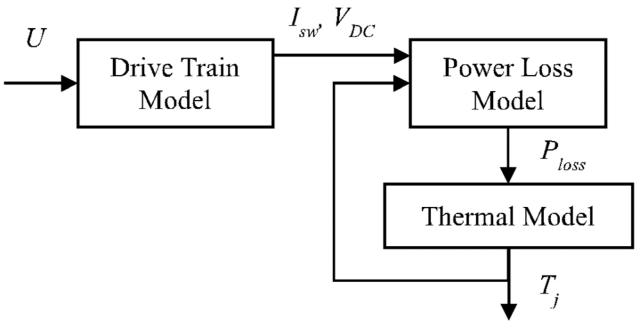

Fig. 2 *Summary of drive train and converter thermal model*

impacts of temporal fidelity and modelling assumptions were explored through an analysis of individual T_j cycles (Section 3.1), comparison of constant wind speed results with a comparable study (Sections 3.2 and 3.3) and analysis of the converter response to synthetic wind speed time series (WSTS) (Section 3.4). A summary of the main findings is given in Section 4.

2 Approach

First, an approach to identifying the thermal loading of a wind turbine power converter was developed as follows:

- Modelling of a wind turbine drive train to provide the current throughput of the converter.
- Modelling of the resultant power losses in the converter due to the current throughput.
- Modelling the power module thermal processes in response to the power losses.
- Simulation of power module thermal response to selected wind speed inputs.

Fig. 2 illustrates the full-system model. U is the incoming wind speed, I_{sw} is the converter switch current, V_{DC} is the DC link voltage, and P_{loss} is the power module device switching losses.

This section outlines the details of each of the sub-systems.

2.1 Drive train model

The drive train model developed for this work was a 2 MW FRC-PMSG, direct-drive turbine. The model was split into five sub-systems: rotor power extraction, drive train dynamics, generator, machine-side converter (MSC), and turbine control. Fig. 3 provides a summary of the drive train model. T_t is the turbine torque extracted from the wind, T_m is the mechanical torque resulting from the shaft stiffness and damping, T_g is the electromagnetic torque, ω_t is the turbine rotational speed, ω_g is the generator rotational speed, β is the pitch angle, β_{ref} is the reference pitch angle, I_{abc} is the generator output current, $V_{t,abc}$ is the generator terminal voltage applied by the MSC, and $V_{ref,abc}$ is the reference MSC output voltages.

This section outlines the core aspects of each sub-system. Detailed descriptions can be found in [17, 18].

2.1.1 Turbine power extraction: T_t from the wind is calculated using the following equation:

$$T_t = \frac{0.5 C_p \rho \pi r^2 U^3}{\omega_t} \tag{1}$$

C_p is the power coefficient, ρ is air density, and r is the turbine radius.

C_p depends on the tip speed ratio (λ) and β. The C_p, λ, and β relationship is turbine specific but it is typical to use a numerical approximation (2) and (3) [19], with λ calculated using (4)

$$\frac{1}{\lambda_i} = \frac{1}{\lambda + H_t \beta} - \frac{K_t}{\beta^3 + 1} \tag{2}$$

$$C_p = A_t \left(\frac{B_t}{\lambda_i} - C_t \beta - D_t \beta^{E_t} - F_t \right) e^{(-G_t/\lambda_i)} \tag{3}$$

$$\lambda = \frac{\omega_t r}{U} \tag{4}$$

A_t to F_t and K_t are turbine specific constants. The values used can be found in the Appendix.

2.1.2 Drive train dynamics: T_t is applied to the drive shaft. The drive train can be modelled as a mechanical mass-spring-damper system which dynamically impacts the T_m applied to the generator.

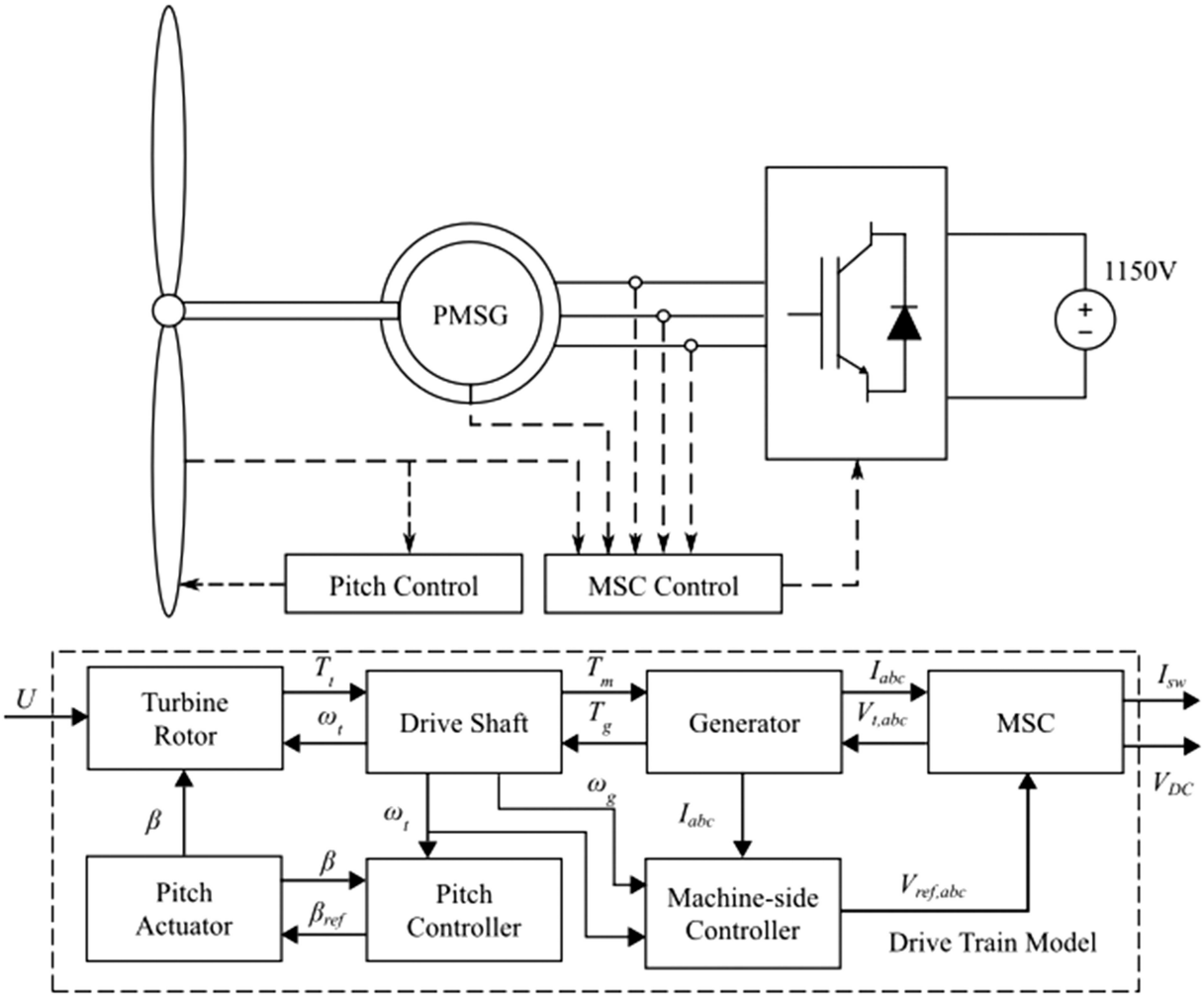

Fig. 3 *Drive train model summary*

The drive train was modelled as a two-mass system, rather than a lumped-mass system, to include the dynamic effects of shaft stiffness and damping. The two-mass system is defined by the following equation [20]:

$$\begin{bmatrix} J_{\mathrm{t}} & 0 \\ 0 & J_{\mathrm{g}} \end{bmatrix} \begin{Bmatrix} \alpha_{\mathrm{t}} \\ \alpha_{\mathrm{g}} \end{Bmatrix} + \begin{bmatrix} C_{\mathrm{d}} & -C_{\mathrm{d}} \\ -C_{\mathrm{d}} & C_{\mathrm{d}} \end{bmatrix} \begin{Bmatrix} \omega_{\mathrm{t}} \\ \omega_{\mathrm{g}} \end{Bmatrix} + \begin{bmatrix} K & -K \\ K & -K \end{bmatrix} \begin{Bmatrix} \theta_{\mathrm{t}} \\ \theta_{\mathrm{g}} \end{Bmatrix} = \begin{Bmatrix} T_{\mathrm{t}} \\ T_{\mathrm{g}} \end{Bmatrix} \quad (5)$$

J_{t}, J_{g} are the moments of inertia of the turbine and generator, respectively, θ_{t}, θ_{g} are the rotational displacements of the turbine and generator, respectively, C_{d} is the shaft damping coefficient, K is the shaft stiffness, and α_{t}, α_{g} are the rotational accelerations of the turbine and generator, respectively. The expanded matrix can be solved numerically, with T_{m} calculated using the following equation:

$$T_{\mathrm{m}} = \left(\omega_{\mathrm{t}} - \omega_{\mathrm{g}}\right) C_{\mathrm{d}} + \left(\theta_{\mathrm{t}} - \theta_{\mathrm{g}}\right) K \quad (6)$$

2.1.3 Generator: The generator model used is a second-order non-salient PMSG in the *dq*0 reference frame [21] with a current rating of 1868 $\mathrm{A_{rms}}$. The mechanical component was modelled with the torque swing equation. The generator parameters can be found in the Appendix.

2.1.4 MSC: In a typical wind turbine, the converter is comprised of an MSC and grid-side converter (GSC). The role of the MSC and GSC differs depending on control strategy but the MSC typically controls the speed of the wind turbine for optimum power production whilst the GSC controls power export to maintain the DC-link voltage.

Due to the turbine's variable speed operation for maximum power extraction, the MSC experiences a more varied operating profile compared with the GSC, which operates at fixed frequency. The MSC is consequently of greater interest for reliability analysis. Here, only the MSC is modelled while the GSC is replaced with a constant voltage source of 1150 $\mathrm{V_{DC}}$ (± 575 $\mathrm{V_{DC}}$).

The MSC parameters were based on the power modules found in the SEMIKRON SKSB2100GD69/11-MAPB stacks [22]. These stacks have a maximum DC voltage of 1200 V and a maximum current of 1000 $\mathrm{A_{rms}}$. The stacks use SKiiP2013GB172-4DWV3 half-bridge integrated power modules [23].

The voltage output of the MSC is determined by $V_{abc,\mathrm{ref}}$ from the machine-side controller (Section 2.1.5). Pulse width modulation (PWM) converts the modulated $V_{abc,\mathrm{ref}}$ (V_{m}) into a switching pattern for the IGBTs in order to produce the three-phase converter output voltage ($V_{\mathrm{c},abc}$). Space vector PWM was chosen and therefore V_{m} was calculated using the following equation:

$$V_{\mathrm{m}} = \frac{\sqrt{3}}{V_{\mathrm{DC}}} V_{abc,\mathrm{ref}} \quad (7)$$

The current through the devices is split between diode and IGBT depending on the current polarity. Since two parallel stacks are required to reach the current rating of the turbine (Section 2.1.3), this current is split equally between stacks [24].

2.1.5 Turbine control: Power extraction is controlled in two ways depending on operating region. Maximum power point tracking (MPPT) is used for below rated speed, while active pitch control is used above rated speed to limit power.

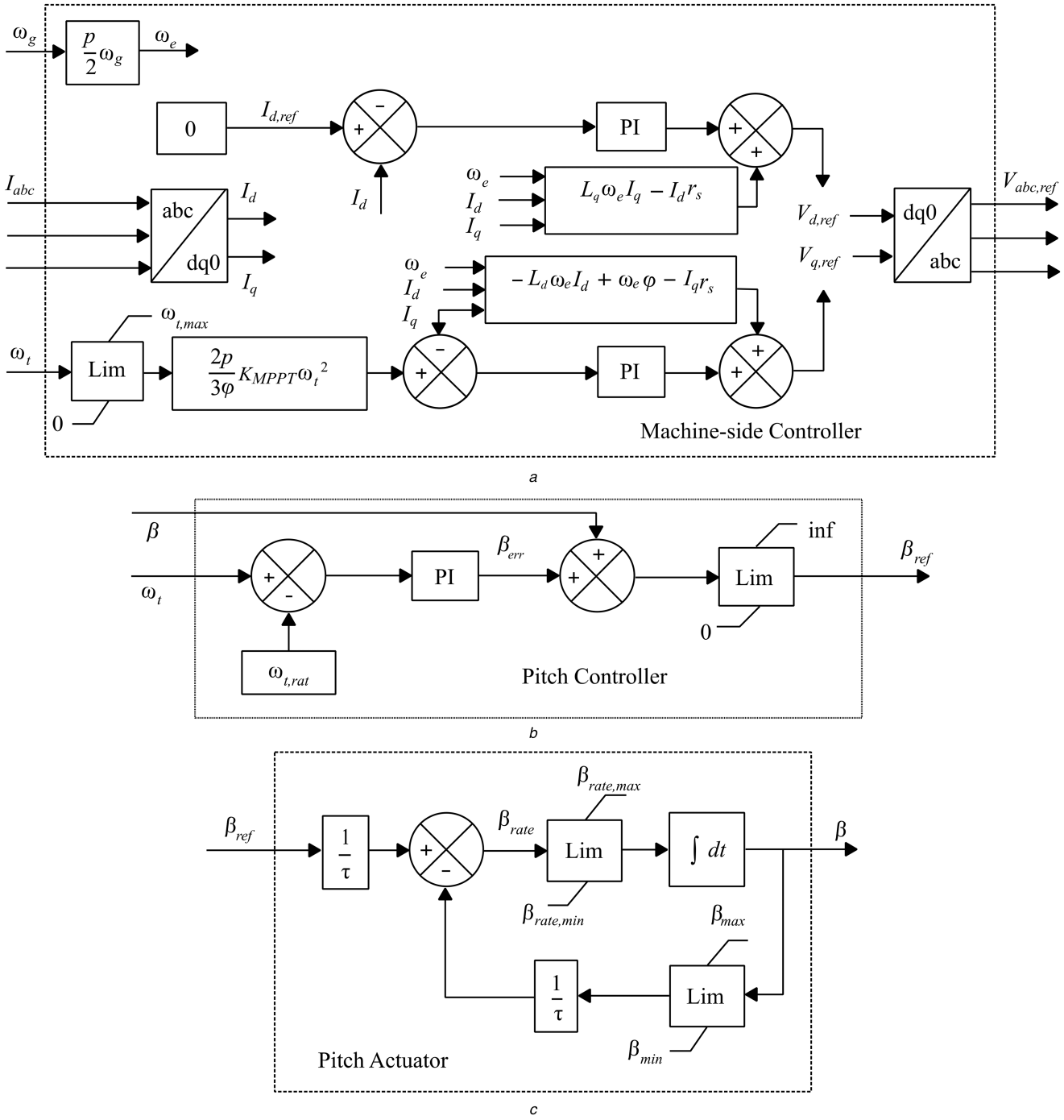

Fig. 4 *Schematics of*
(a) Machine side controller, ***(b)*** Pitch controller, ***(c)*** Pitch actuator

For MPPT, C_p must be maximised ($C_{p,max}$). By controlling ω_t, the optimum λ can be maintained (λ_{opt}) when below rated wind speed

$$\omega_{t,opt(u)} = \frac{U\lambda_{opt}}{r} \tag{8}$$

$\omega_{t,opt(u)}$ is the optimum turbine rotational speed at a given wind speed.

As U is not measured in this control strategy, $\omega_{t,opt}$ is unknown. Instead ω_t is varied until the turbine reaches steady state, which occurs when $\omega_t = \omega_{t,opt}$. ω_t is varied via T_g, which is carried out using direct-quadrature-zero current (I_{dq0}) control applied to the MSC. Fig. 4*a* illustrates the machine-side control algorithm. $V_{d,q}$ are the d,q reference frame voltages, $V_{d,q,ref}$ are the required d,q terminal voltages, $I_{d,q,ref}$ are the reference $I_{d,q}$, r_s is the PMSG stator phase resistance, $L_{d,q}$ are the PMSG d,q armature inductances, φ is the permanent magnet flux linkage, K_{MPPT} is a turbine specific constant, $\omega_{t,max}$ is the maximum turbine rotational speed considered by the controller, and ω_e is the magnetic field rotational speed, which is related to ω_g via the generator pole pairs.

To determine the required generator currents, ω_t is related to the required T_g (T_{ref}) via the turbine power curve using a turbine specific constant K_{MPPT} (9) and (10). The reference I_q is calculated using a known relationship between I_q and T_g in the generator (11). I_d is maintained at 0 A [25]. These currents are achieved by applying a controlled voltage on the generator terminals using the MSC

$$T_{ref} = K_{MPPT}\omega_t^2 \tag{9}$$

$$K_{\mathrm{MPPT}} = 0.5 C_{p,\max} \rho \pi r^2 \left(\frac{r}{\lambda_{\mathrm{opt}}} \right)^3 \tag{10}$$

$$I_{q,\mathrm{ref}} = \frac{2p}{3\varphi} T_{\mathrm{ref}} \tag{11}$$

To note, the machine-side controller is not constrained by the rated turbine rotational speed ($\omega_{\mathrm{t,rat}}$) but by a higher maximum ($\omega_{\mathrm{t,max}}$). This allows the machine-side controller to deal with sudden increases in wind speed for which the pitch controller is too slow to respond effectively. This provides a similar controller interaction to [26].

Pitch control limits power extraction when above rated wind speed by pitching the blades away from the optimum angle, reducing the turbine's C_{p}.

There are a number of pitch control methods available [27]. For this work, the difference in ω_{t} and rated ω_{t} ($\omega_{\mathrm{t,rat}}$) is used to produce a β error (β_{err}) (Fig. 4*b*). β_{err} is added to the current β to produce a reference β (β_{ref}) and applied to the pitch actuator (Fig. 4*c*). The pitch actuator is modelled as a first-order dynamic system [28] with limits on β and the rate of change of β (β_{rate}). These values can be found in the Appendix.

2.1.6 Drive train model summary: The drive train model consists of the following key features:

- Modelled as a direct-drive 2 MW PMSG wind turbine to align with modern turbine technology with sufficient data for modelling.
- Mechanical drive train modelled as a two-mass model to capture the critical dynamics of a wind turbine drive train.
- FRC with MSC based on SEMIKRON Renewable Energy stacks to provide realistic converter parameters.
- GSC modelled as an ideal DC link to isolate impacts of wind on the MSC.
- Turbine controlled using ω_{t} as the reference signal, with both MPPT and active pitch control as in the majority of modern wind turbines.

2.2 Converter power loss model

To convert the current throughput into T_{j} profiles, power losses must be calculated, specifically:

- The IGBT and diode conduction losses.
- The IGBT switching losses and diode reverse recovery (RR) losses.

The conduction and switching losses are summed for each device. The power loss model used is based on [29, 30].

2.2.1 Conduction losses: Conduction losses depend on device internal resistance so are calculated using the device voltage and current

$$P_{\mathrm{C,IGBT}} = V_{\mathrm{ce}} I_{\mathrm{c}} \tag{12}$$

$$P_{\mathrm{C,diode}} = V_{\mathrm{f}} I_{\mathrm{f}} \tag{13}$$

$P_{\mathrm{C,IGBT}}$ and $P_{\mathrm{C,diode}}$ are the IGBT and diode conduction losses, respectively, V_{ce} is the IGBT collector–emitter voltage, V_{f} is the diode forward voltage, I_{c} is the IGBT collector current, and I_{f} is the diode forward current.

I_{c} and I_{f} are the input currents. V_{ce} and V_{f} are functions of I_{c} and I_{f}, respectively, and the device T_{j}. The functions are given in the manufacturer's data sheet [23] for a T_{j} of 25 and 125°C. V_{ce} and V_{f} are calculated by interpolating between the values given at these reference temperatures.

2.2.2 Switching/RR losses: Switching and RR losses occur when there is a change in direction of voltage and current. Device response is not instantaneous but occurs over nanoseconds [29]. Nanosecond simulation is impractical for run times longer than a few seconds and the energy loss information given in manufacturer's datasheets is not detailed enough for accurate temporal loss simulation. For example, the energy loss during switch on (E_{on}) and switch off (E_{off}) are not given separately, but reported as a summation of the two ($E_{\mathrm{on+off}}$) [23]. As such, a simplified approach has to be taken.

It has been assumed that the energy loss is given by the conditions at the first low-high (L-H) switching instance. The energy is modulated over the switching cycle (between L-H and the next L-H) to provide a constant switching power loss. This was deemed acceptable as the device thermal time constants (µs-ms) will dominate the thermal profile [29].

With the above assumptions, the switching/RR losses were found by

(i) Determining the energy losses at L-H switching events. The switching/RR energy loss is given as a function of input current at two reference V_{DC} [23] and is assumed to be linear. The IGBT energy loss is $E_{\mathrm{on+off}}$, whilst the diode energy loss is twice the reverse energy loss (E_{rr}).

(ii) Calculating the equivalent modulated power losses over the switching cycle using the following equations [30]:

$$P_{\mathrm{sw}}\left(t : T_{\mathrm{s,th}} : \left(t + T_{\mathrm{p,sw}}(t)\right)\right) = \frac{E_{\mathrm{on+off}}(t)}{T_{\mathrm{p,sw}}(t)} \tag{14}$$

$$P_{\mathrm{rr}}\left(t : T_{\mathrm{s,th}} : \left(t + T_{\mathrm{p,rr}}(t)\right)\right) = \frac{E_{\mathrm{rr}}(t)}{T_{\mathrm{p,rr}}(t)} \tag{15}$$

$$P_{\mathrm{sw},T_{\mathrm{j}}}(t) = \left(1 + TC_{E\mathrm{sw}}\left(T_{\mathrm{j,IGBT}}(t) - T_{\mathrm{ref}}\right)\right) P_{\mathrm{sw}}(t) \tag{16}$$

$$P_{\mathrm{rr},T_{\mathrm{j}}}(t) = \left(1 + TC_{E\mathrm{rr}}\left(T_{\mathrm{j,diode}}(t) - T_{\mathrm{ref}}\right)\right) P_{\mathrm{rr}}(t) \tag{17}$$

P_{sw} is the IGBT switching power loss, P_{rr} is the diode RR power loss, t is the time step, $T_{\mathrm{s,th}}$ is the thermal sampling time, $T_{\mathrm{p,sw}}$ is the IGBT switching time period, $T_{\mathrm{p,rr}}$ is the diode RR time period, $P_{\mathrm{sw},Tj}$, $P_{\mathrm{rr},Tj}$ are the T_{j} corrected P_{sw} and P_{rr}, respectively, $\mathrm{TC}_{E\mathrm{sw}}$, $\mathrm{TC}_{E\mathrm{rr}}$ are the switching loss and RR temperature coefficients, respectively, and T_{ref} is the reference temperature of the energy loss look-up tables (LUTs).

2.3 Thermal loss model

Converter thermal modelling can be carried out in three ways:

- Thermal equivalent circuits using resistor–capacitor (RC) networks [8, 10–12, 14–16].
- Thermal diffusion equations [13].
- Finite-element analysis [7].

As the RC network data was readily available, a common practice approach of thermal equivalent circuit modelling was used.

The data given in [23] is for a Foster RC network. To provide a more accurate half-bridge temperature profile the Foster thermal resistance ($R_{\mathrm{th,f}}$) and time constant (τ) parameters were converted into RC parameters [31], and then converted into Cauer RC parameters to provide a more realistic thermal profile throughout the device [32]. Fig. 5 gives the half-bridge Cauer RC network. The parameters are available in the Appendix.

The power losses (P_{loss}) are dependent on T_{j} and therefore the power loss and thermal sub-systems must be run concurrently. Due to the power-thermal inter-dependency, the initialisation of C_{th} temperatures was solved iteratively. The steady-state temperatures are related to the R_{th} only [30]. Therefore, initial temperatures were

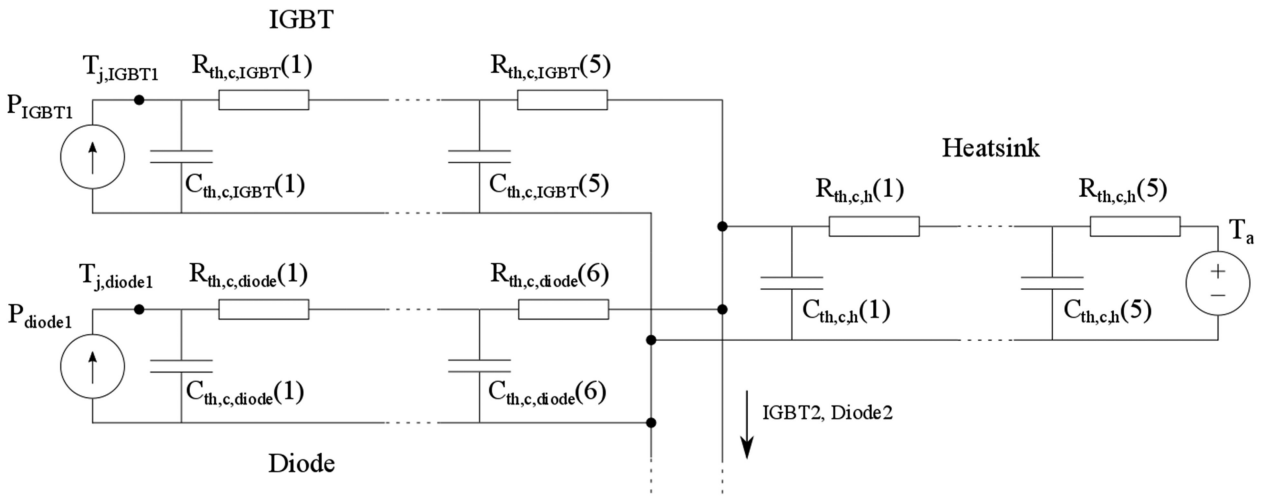

Fig. 5 *Half-bridge Cauer RC network (one IGBT and diode represented). P_{IGBT1} is the IGBT power loss, P_{diode1} is the diode power loss, $R_{th,c}$ is the Cauer thermal resistance, and $C_{th,c}$ is the Cauer thermal capacitance*

set throughout the device, and then the power losses and temperatures were iteratively updated until steady state was reached.

2.4 Wind speed inputs

Wind speed and converter current throughput are partly decoupled by the drive train inertia and control [17]. As such, it can be challenging to determine which characteristics of a WSTS have the largest impact on thermal loading.

To address this, experiments have been constructed which use synthetic WSTS to isolate potential wind speed characteristics and determine their impact on thermal loading. Square waves have been used to represent sudden changes in wind speed, which was validated against high-frequency wind speed data. The tests are carried out over 65 s, with the first 5 s carried out at constant wind speed to minimise the impact of variations in the input current. For the square wave tests this constant wind speed represents the average power wind speed, which is slightly higher than the average wind speed. The model time step is also much smaller than the test period to ensure it does not influence the results; 5×10^{-6}s for the drive train, and 5×10^{-5}s for the thermal simulation.

2.5 Summary

To summarise, a Simulink model of a wind turbine drive train and power converter thermal network has been constructed. This allows for any wind speed profile to be entered and the corresponding power module thermal profiles be produced.

3 Results and discussion

This section outlines the analysis performed on T_j profiles produced in response to constant and square wave WSTS.

3.1 Individual T_j cycles

The power loss and temperature profiles over individual power cycles were examined. Fig. 6 compares the diode and IGBT current T_j profiles at a constant 12.7 m/s. The T_j profile for the diode (Fig. 6*d*) is comparable with the expected response found in Fig. 5.2.13 in the manufacturer's handbook [30], although it should be noted that the manufacturer's data considers only the average power loss of the switching cycle, rather than individual switching events. This simulation output can show higher frequency temperature variation than revealed in the manufacturer's data.

This higher frequency temperature variation becomes most apparent in the IGBT (Fig. 6*c*), particularly in the first half of the current cycle. This can be attributed to the converter being connected to a PMSG. The PMSG reactance causes the current to be out-of-phase with the voltage, and therefore the switching cycles are not distributed symmetrically over the input current, with a period of low voltage (Fig. 6*a*). The low voltage means the IGBT has a smaller duty cycle. Where there is infrequent current due to a low duty cycle (Fig. 6*a*), T_j varies more (Fig. 6*c*). This effect is not seen in the diode as the current not flowing through the IGBT must pass through the diode, creating a near continuous current throughput (Fig. 6*b*) and therefore a smooth T_j response (Fig. 6*d*).

3.2 Constant wind speeds

Fig. 7 shows the thermal response to constant WSTS for an IGBT and diode with an ambient temperature (T_a) of 40°C [8]. The mean T_j increases non-linearly as wind speed increases due to the cubic relationship between wind speed and power. The ΔT_j also increases due to the higher power loss per cycle, and the ΔT_j frequency increases due to the higher generator rotational speed.

The diode temperatures T_j and ΔT_j (Fig. 7*b*) are consistently higher than the IGBT (Fig. 7*a*). This is due to the higher power losses experienced by the diodes and the higher R_{th} of the diodes. The higher diode R_{th} (K/W) means that for every watt of heat loss, the diode experiences a greater rise in temperature than the IGBT. This is then coupled with the greater power losses due to the more continuous current flow through the diode (Section 3.1), causing the higher T_j and ΔT_j. This was also found for the MSC devices in [14] and suggests that the diode is more vulnerable to thermal cycling, with both higher mean T_j and ΔT_j.

3.3 Study comparison

The results in Figs. 7*a* and *b* were compared with the 1.55 MW turbine in [14] (Fig. 7*c*); it is assumed the scaled power ratings would have limited impact on the thermal loading as the converter rating would also be scaled, leading to comparable T_j profiles for a given wind speed. However, whilst it was found that the ΔT_j for both IGBTs and diodes was comparable at a given wind speed, the mean T_j for a given wind speed was higher in this study than in [14], despite T_a being 10°C lower. This is in part is due to the lack of R_{th} value for the heatsink in [14]. At steady-state conditions this will create a higher case temperature (T_c) and therefore higher mean T_j. The mean T_j change from 12 to 8.5 m/s is also much lower in [14]. This suggests that the MSC in this work is more susceptible to T_j rises due to the higher R_{th} values in the devices. This highlights three key conclusions that must be made.

- The ΔT_j magnitude for IGBT and diodes is consistent with those found in [14], but there is greater variation in mean T_j between wind speeds in this study.

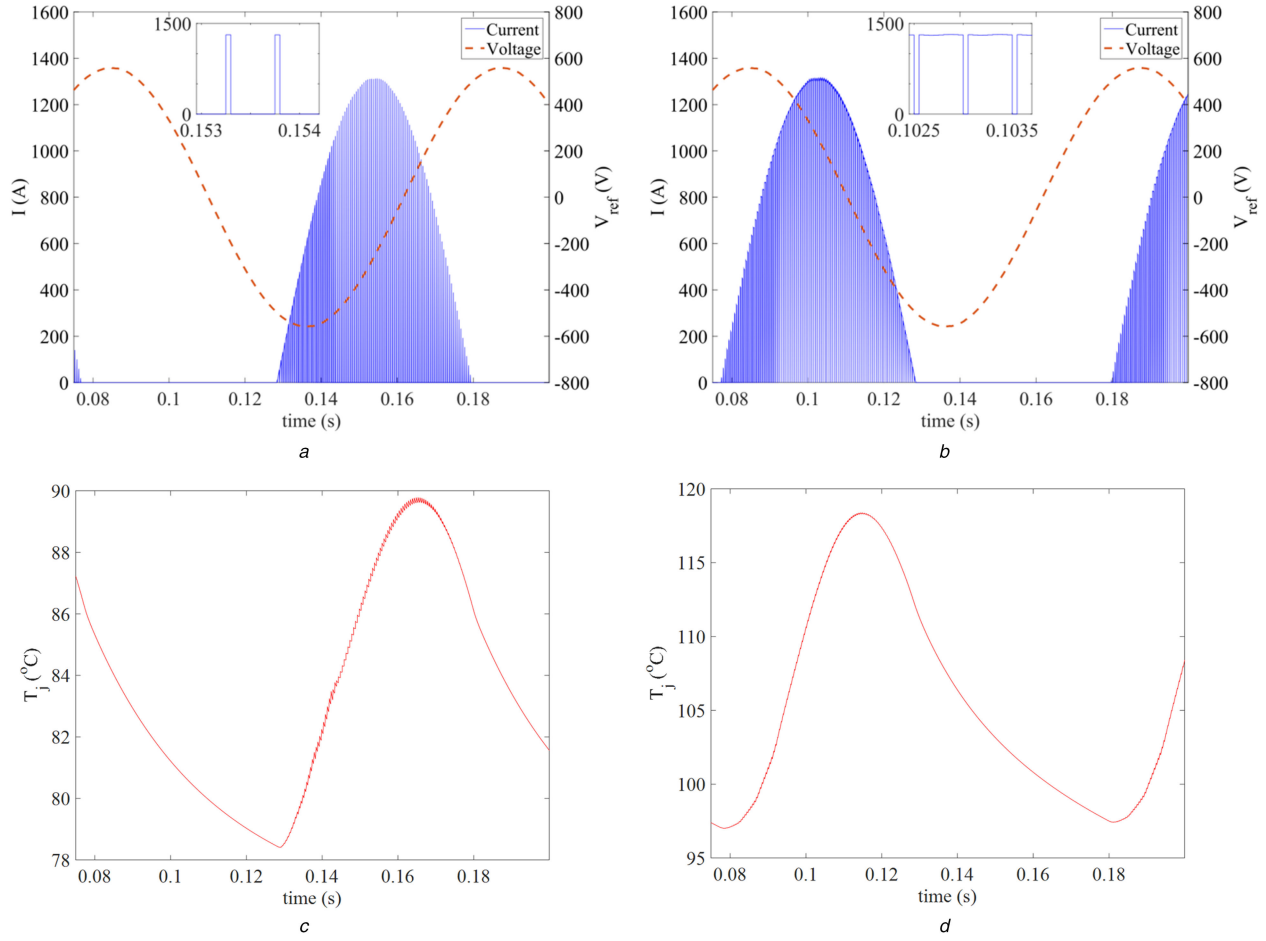

Fig. 6 *Cycle view of*
(a) IGBT current with the current waveform peak magnified, ***(b)*** Diode current with the current waveform peak magnified, ***(c)*** IGBT T_j, ***(d)*** Diode T_j at a constant 12.7 m/s

- The value of T_a can have a large impact on the mean T_j value.
- The inclusion of the heatsink thermal parameters in the model causes a significant increase in the mean T_j.

3.4 Response to varying wind speed input

The T_j response of the power module to a range of square wave WSTS is detailed to understand what might be masked by using SCADA data in lifetime/temperature swing calculations. For comparison, the maximum T_j swing over the simulation period (max ΔT_j) have been plotted for square gust amplitudes of 1 and 2 m/s, for varying frequencies and mean wind speeds, for both IGBT and diode (Fig. 8).

In general, the higher the frequency of wind speed variation, the lower ΔT_j becomes. This is as the turbine inertia acts as a low-pass filter, restricting the high-frequency wind speed variation being transmitted as current variation. Indeed, wind speed variations with frequency >0.25 Hz lead to a minimal increase in ΔT_j compared with the constant wind speed case (0 Hz). Therefore, reasonable approximations of T_j profiles can be made (within 1°C) with 0.25 Hz wind speed data. Furthermore, these results imply that lower turbulence wind farm sites, such as offshore, have more damaging thermal profiles in the converter than higher turbulence onshore sites.

There are exceptions to this trend. ΔT_j becomes relatively consistent below 0.03 Hz. This is because the turbine has time to respond to the change of wind speed and reaches its steady operating state. The turbine is then at this steady-state condition long enough for T_j to reach its maximum before the wind speed reduces. Lower frequencies will increase the number of times that the maximum T_j is reached during a particular gust, but will not affect the maximum T_j. The same will also be true for the minimum T_j. Therefore, gust frequencies of 0.03 Hz and below provide the maximum ΔT_j.

These results show that the use of one wind speed data point for a long time period, e.g. 10 min SCADA data, 3 hourly data found in [11], or the use of a wind speed distribution in [8, 10], can mask a large amount of information and will underestimate the T_j variation significantly; in Fig. 8*d* the diode ΔT_j at U_m of 12 m/s increases by up to 71%. Therefore, these results agree with the conclusions in [15] that higher frequency wind speed data is required for accurate T_j profile estimation, and it is suggested that a minimum WSTS frequency of 0.25 Hz is required, though it is recognised that this will not always be available/practical. This, however, would reduce the amount of data required for studies such as in [12–15]. The results at higher U_m also indicate that the unique operating conditions may have a significant effect on the T_j profile experienced by the power converter, and therefore the lack of drive train dynamic modelling in [7–9] will change the T_j profiles significantly.

4 Conclusions

The power converter is reliability critical for FRC-PMSG wind turbines. Converter failures are typically linked to the thermal loading of the power module. This paper models the converter thermal loading when the turbine is subjected to various synthetic WSTS to explore and demonstrate the impact of the frequency of wind speed variation on power converter thermal loading.

The thermal simulation has three main parts: a PMSG drive train model, a converter power loss model based on conduction and switching/RR, and a thermal equivalent circuit model. Both constant and square wave WSTS were tested to replicate real wind characteristics. From the results, it can be concluded that:

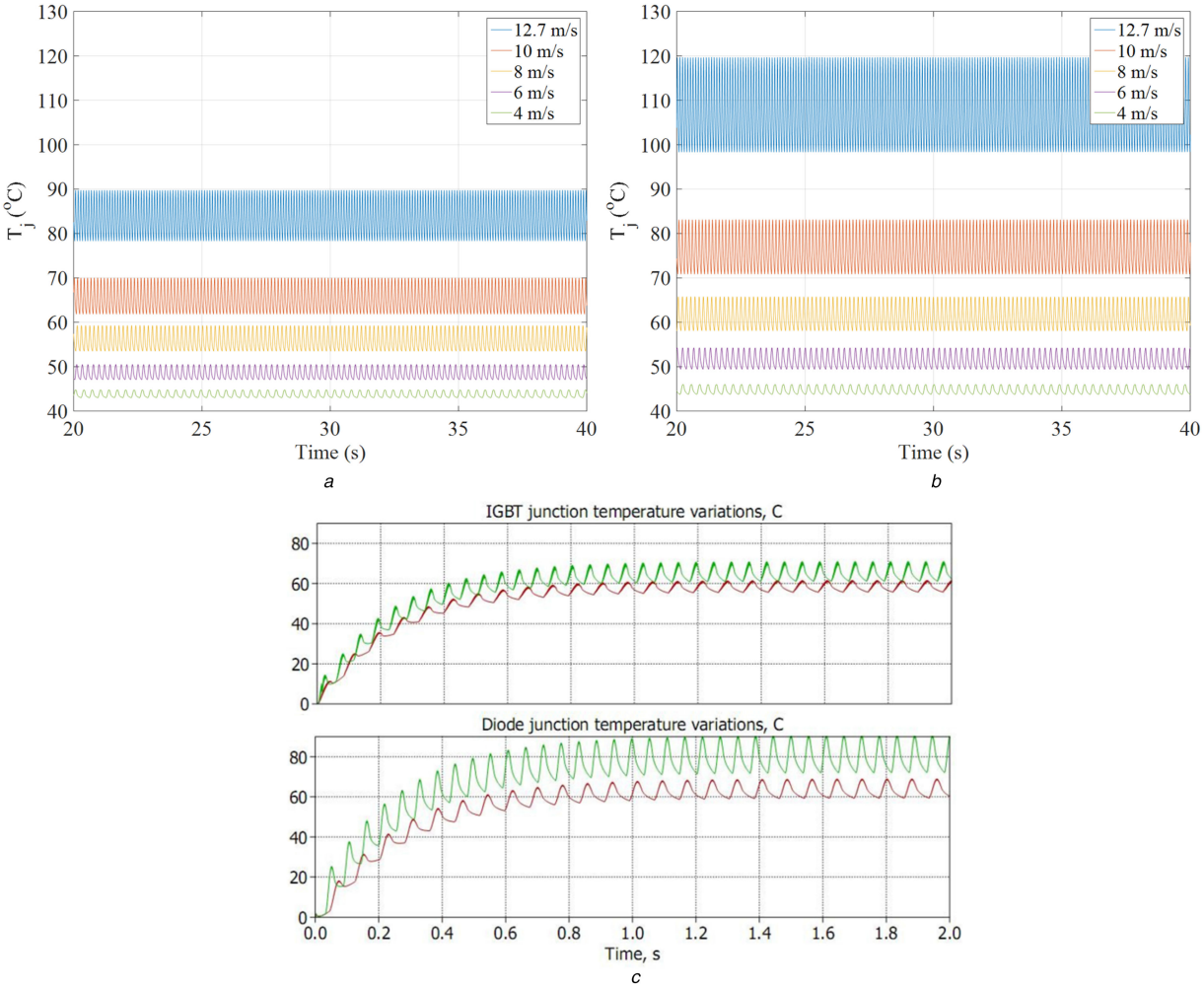

Fig. 7 *T_j response to constant wind speeds in the MPPT region for*
(a) IGBT, ***(b)*** Diode, ***(c)*** Results found in [14] for a 12 m/s input

- At high wind speeds the switching pattern of the IGBT causes intermittent T_j profiles.
- The diodes experience greater thermal loading than the IGBTs in all comparative cases.
- A comparison with another study showed that the inclusion of heat sink thermal parameters and ambient temperature are important for providing accurate T_j profiles.
- The lower the frequency of wind speed variation, the higher ΔT_j becomes, implying that low turbulence sites such as offshore have greater thermal variation, and therefore damage, in the converter.
- For the first time, the minimum wind speed data frequency for accurate converter thermal simulation has been determined. Wind speed variations with frequency >0.25 Hz have a small increase in ΔT_j and therefore reasonable approximations of T_j profiles can be made with 0.25 Hz wind speed data. Wind speed data at lower frequencies allow simulations to overlook damaging temperature variations.

5 Acknowledgments

This work was supported by the EPSRC SUPERGEN Wind project (grant number EP/L014106/1).

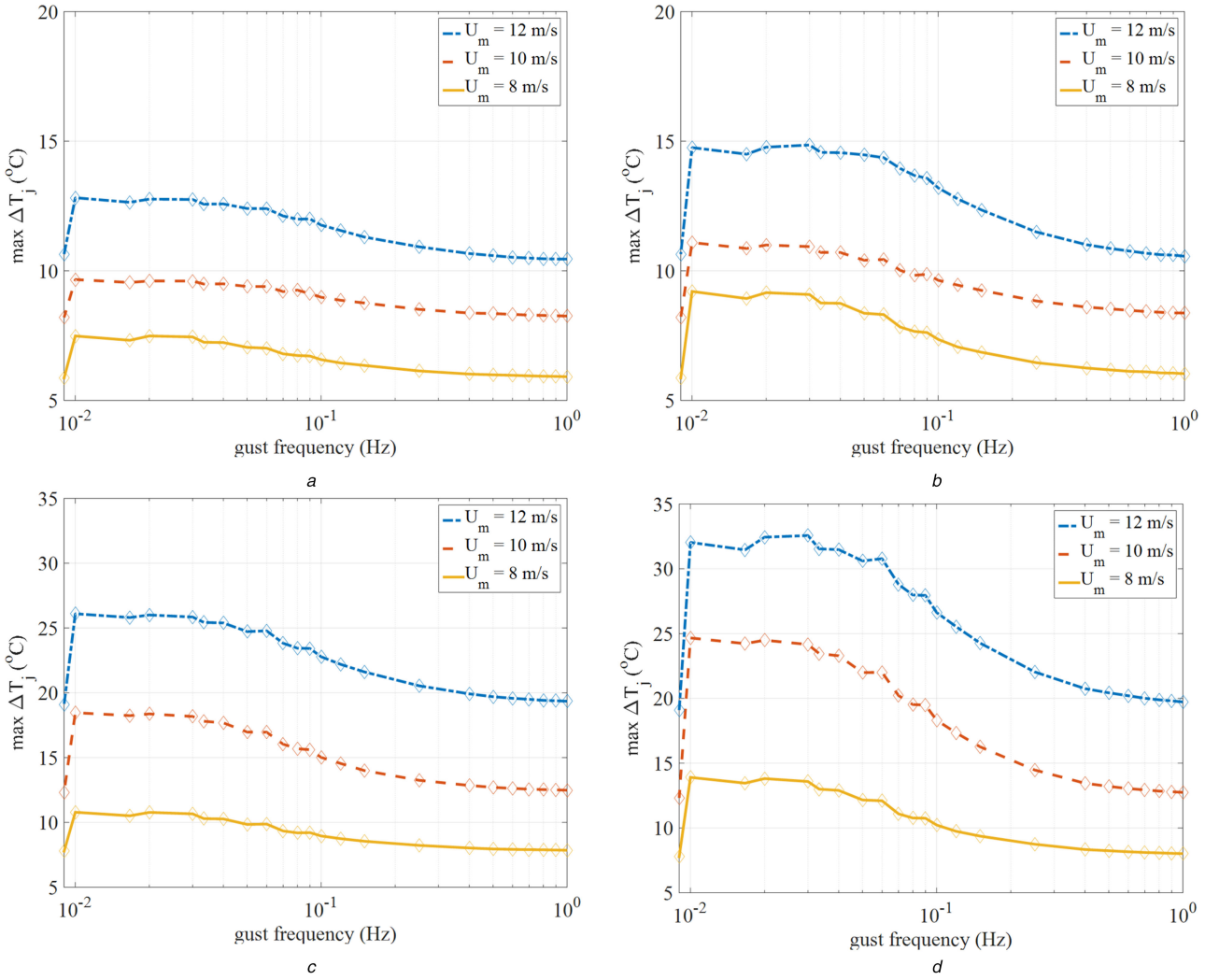

Fig. 8 *Max ΔT_j over varying mean wind speeds (U_m) and square gust frequencies for*
(a) IGBT for ΔU of 1 m/s, ***(b)*** IGBT for ΔU of 2 m/s, ***(c)*** Diode for ΔU of 1 m/s, ***(d)*** Diode for ΔU of 2 m/s

6 References

[1] 'Offshore Wind Cost Reduction, Pathways Study. Available at http://www.thecrownestate.co.uk/media/5493/ei-offshore-wind-cost-reduction-pathways-study.pdf, accessed 19 July 2016

[2] 'Large-Scale Offshore Wind Power in the United States: Assessment of Opportunities and Barriers'. Available at http://www.nrel.gov/docs/fy10osti/40745.pdf, accessed 19 July 2016

[3] Carroll, J., McDonald, A., McMillan, D.: 'Failure rate, repair time and unscheduled O&M cost analysis of offshore wind turbines', *Wind Energy*, 2015, **19**, (6), pp. 1107–1119

[4] Carroll, J., McDonald, A., McMillan, D.: 'Reliability comparison of wind turbines with DFIG and PMG drive trains', *IEEE Trans. Energy Convers.*, 2015, **30**, (2), pp. 663–670

[5] Spring, M., Davies, P., Gaal, G., *et al.*: 'Top 30 Chart for wind turbine failure mechanisms'. EWEA Annual Event, Paris, France, November 2015

[6] 'Application Manual Power Semiconductors'. Available at https://www.semikron.com/dl/service-support/downloads/download/semikron-application-manual-power-semiconductors-english-en-2015, accessed 8 September 2016

[7] Bartram, M., De Doncker, R.: 'Doubly-fed-machines in wind-turbine systems: is this application limiting the lifetime of IGBT-frequency-converters?'. IEEE PESC, Aachen, Germany, June 2004, pp. 2583–2587

[8] Fuchs, F., Mertens, A.: 'Steady state lifetime estimation of the power semiconductors in the rotor side converter of a 2 MW DFIG wind turbine via power cycling capability analysis'. EPE, Birmingham, UK, August 2011

[9] Weiss, D., Eckel, H.: 'Fundamental frequency and mission profile wearout of IGBT in DFIG converters for windpower'. EPE, Lille, France, September 2013

[10] Zhou, D., Blaaberg, F., Franke, T., *et al.*: 'Reliability and energy loss in full-scale wind power converter considering grid codes and wind classes'. IEEE ECCE, Pittsburgh, USA, September 2014, pp. 3067–3074

[11] Kostandyan, E., Ma, K.: 'Reliability estimation with uncertainties consideration for high power IGBTs in 2.3 MW wind turbine converter system', *Microelectron. Reliab.*, 2012, **52**, (9), pp. 2403–2408

[12] Ma, K., Liserre, M., Blaabjerg, F., *et al.*: 'Thermal loading and lifetime estimation for power device considering mission profiles in wind power converter', *IEEE Trans. Power Electron.*, 2015, **30**, (2), pp. 590–602

[13] Mussallam, M., Johnson, C.: 'Impact of different control schemes on the life consumption of power electronic modules for variable speed wind turbines'. EPE, Birmingham, UK, August 2011

[14] Baygildina, E., Peltoniemi, P., Pyrhönen, O., *et al.*: 'Thermal loading of wind power converter considering dynamics of wind speed'. IEEE IECON, Vienna, Austria, November 2013, pp. 1362–1367

[15] Isidoril, A., Rossi, F., Blaaberg, F., *et al.*: 'Thermal loading and reliability of 10-MW multilevel wind power converter at different wind roughness classes', *IEEE Trans. Ind. Appl.*, 2014, **50**, (1), pp. 484–494

[16] Senturk, O., Munk-Nielsen, S., Teodorescu, R., *et al.*: 'Electro-thermal modeling for junction temperature cycling-based lifetime prediction of a press-pack IGBT 3L-NPC-VSC applied to large wind turbines'. IEEE ECCE, Phoenix, USA, September 2011, pp. 568–575

[17] Smith, C., Wadge, G., Crabtree, C., *et al.*: 'Characterisation of electrical loading experienced by a nacelle power converter'. EWEA Annual Event, Paris, France, November 2015

[18] Smith, C., Crabtree, C., Matthews, : 'Impact of wind conditions on thermal loading of PMSG wind turbine power converter'. IET PEMD, Glasgow, UK, April 2016

[19] Heier, S.: '*Grid integration of wind energy: onshore and offshore conversion systems*' (John Wiley & Sons, 2014, 3rd edn.)

[20] Rao, S., Yap, F.: '*Mechanical vibrations*' (Addison-Wesley, 1995)

[21] Wu, B., Lang, Y., Kouro, S.: '*Power conversion and control of wind energy systems*' (John Wiley & Sons, 2011)

[22] 'SKS B2 100 GD 69/11 - MA PB Datasheet'. Available at http://www.semikron.com/dl/service-support/downloads/download/semikron-datasheet-sks-b2-100-gd-69-11-ma-pb-08800565, accessed 7 December 2015

[23] 'SKiiP 2013 GB172-4DW V3 Datasheet'. Available at http://www.semikron.com/dl/service-support/downloads/download/semikron-datasheet-skiip-2013-gb172-4dw-v3-20451248, Accessed 8 December 2015

[24] 'Optimised Converter for Solar and Wind'. Available at http://www.semikron.com/dl/service-support/downloads/download/semikron-flyer-semistackre-2014-04-08, accessed 14 September 2015

[25] Anaya-Lara, O., Jenkins, N., Ekanayake, J., *et al.*: '*Wind energy generation: modelling and control*' (John Wiley & Sons, 2009)

[26] Hansen, A., Sorensen, P., Iov, F., *et al.*: 'Control of variable speed wind turbines with doubly-fed induction generators', *Wind Eng.*, 2004, **28**, pp. 411–432

[27] Zhang, J., Cheng, M., Chen, Z., *et al.*: 'Pitch angle control for variable speed wind turbines'. DPRT, Nanjuing, China, April 2008, pp. 2691–2696
[28] Bianchi, F., De Battista, H., Mantz, R.: '*Wind turbine control systems: principles, modelling and gain scheduling design*' (Springer Science & Business Media, 2006)
[29] Wyllie, P.: 'Electrothermal modelling for doubly fed induction generator converter reliability in wind power'. Durham University thesis, 2014
[30] Wintrich, A., Nicolai, U., Tursky, W., *et al.*: 'Application manual power semiconductors' (SEMIKRON International GmBH, 2015)
[31] 'AN11261: Using RC Thermal Models: Application note'. Available at http://www.nxp.com/documents/application_note/AN11261.pdf, accessed 9 December 2015
[32] 'Convert Foster Network to Cauer'. Available at http://uk.mathworks.com/matlabcentral/fileexchange/46348-convert-foster-network-to-cauer/content//fostercauer.m, accessed 9 December 2015
[33] Slootweg, J., Polinder, H., Kling, W.: 'Dynamic modelling of a wind turbine with doubly fed induction generator'. PESSM, Canada, July 2001, pp. 644–649
[34] Akhmatov, V.: 'Analysis of dynamic behaviour of electric power systems with large amount of wind power'. Technical University of Denmark thesis, 2003
[35] Sim, J., Kim, K., Son, R., *et al.*: 'Ride-through of PMSG wind power system under the distorted and unbalanced grid voltage dips', *J. Electr. Eng. Technol.*, 2012, **7**, (6), pp. 898–904
[36] Leithead, W., Connor, B.: 'Control of variable speed wind turbines: dynamic models', *Int. J. Control.*, 2000, **73**, (13), pp. 1173–1188
[37] Gonzalez-Longatt, F., Wall, P., Terzija, V.: 'A simplified model for dynamic behavior of permanent magnet synchronous generator for direct drive wind turbines'. IEEE PES PowerTech, Trondheim, June 2011, pp. 1–7

7 Appendix

$P_{t,rat}$ is the rated turbine power, f_{rat} is the rated frequency, U_{rat} is the rated wind speed, $V_{l,rat}$ is the rated line voltage, I_{rat} is the rated current, T_{rat} is the rated torque, V_f is the IGBT forward voltage, V_{fd} is the diode forward voltage, $T_{f,t}$ is the IGBT fall time and tail time, respectively, R_{on} is the IGBT on-state slope resistance, $P_{p,id,iq}$ are the proportional gains for the pitch, I_d, and I_q controllers, respectively, $I_{p,id,iq}$ are the integral gains for the pitch, I_d, and I_q controllers, respectively, and f_{sw} is the switching frequency (see Table 1).

Table 1a *Continued*

Parameter	Value	Reference
A_t	0.22	[33]
B_t	116	[33]
C_t	0.4	[33]
D_t	0	[33]
E_t	0	[33]
F_t	5	[33]
G_t	12.5	[33]
H_t	0.08	[33]
K_t	0.035	[33]
$P_{t,rat}$	2.0 MW	[21]
$\omega_{t,rat}$	22.5 rpm	[21]
f_{rat}	9.75 Hz	[21]
λ_{opt}	6.3	—
$C_{p,max}$	0.438	—
U_{rat}	12.7 m/s	—
r	34 m	—
ρ	1.225 kg/m^3	[25]
J_t	2.92×10^6 kg/m^2	[34]
J_g	200 kg/m^2	[35]
K	4.0×10^7 Nm/rad	[34]
C_d	6.72×10^6 Nms/rad	—
$V_{l,rat}$	690 $V_{(rms)}$	[21]
$I_{,rat}$	1867.76 $A_{(rms)}$	[21]
T_{rat}	848.826 kNm	[21]
R_s	8.21×10^{-4} Ω	[23]
L_d	1.5731 mH	[23]
p	52	[23]
φ	8.24 Vs (peak)	[23]
V_f	0.95 V	[23]
V_{fd}	1.9 V	[23]
R_{on}	0.925 mΩ	[23]
V_{DC}	1150 V	—
β_{max}	45°	[36]
β_{min}	0°	[36]
$\beta_{rate,max}$	8°/s	[36]
$\beta_{rate,min}$	−8°/s	[36]
τ	0.5 s	[37]
P_p	3.357	—
I_p	0.012	—

Table 1b *Drive train parameters*

Parameter	Value	Reference
P_{id}	−0.148	—
I_{id}	−5.377	—
P_{iq}	−0.155	—
I_{iq}	−2.689	—
f_{sw}	2 kHz	[22]
$R_{th,c,IGBT}(1)$	1.5×10^{-3} K/W	—
$R_{th,c,IGBT}(2)$	7.3×10^{-3} K/W	—
$R_{th,c,IGBT}(3)$	5.9×10^{-3} K/W	—
$R_{th,c,IGBT}(4)$	2.5×10^{-3} K/W	—
$R_{th,c,IGBT}(5)$	0.37×10^{-3} K/W	—
$C_{th,c,IGBT}(1)$	0.55 Ws/K	—
$C_{th,c,IGBT}(2)$	3.61 Ws/K	—
$C_{th,c,IGBT}(3)$	35.90 Ws/K	—
$C_{h,c,IGBT}(4)$	476.61 Ws/K	—
$C_{h,c,IGBT}(5)$	4.81×10^3 Ws/K	—
$R_{th,c,diode}(1)$	2.8×10^{-3} K/W	—
$R_{th,c,diode}(2)$	10.2×10^{-3} K/W	—
$R_{th,c,diode}(3)$	10.5×10^{-3} K/W	—
$R_{th,c,diode}(4)$	11.9×10^{-3} K/W	—
$R_{th,c,diode}(5)$	8.6×10^{-3} K/W	—
$R_{th,c,diode}(6)$	0.94×10^{-3} K/W	—
$C_{th,c,diode}(1)$	0.773 Ws/K	—
$C_{th,c,diode}(2)$	1.45 Ws/K	—
$C_{th,c,diode}(3)$	4.90 Ws/K	—
$C_{th,c,diode}(4)$	36.07 Ws/K	—
$C_{th,c,diode}(5)$	577.76 Ws/K	—
$C_{th,c,diode}(6)$	1.60×10^4 Ws/K	—
$R_{th,c,h}(1)$	0.79×10^{-3} K/W	—
$R_{th,c,h}(2)$	3.1×10^{-3} K/W	—
$R_{th,c,h}(3)$	4.3×10^{-3} K/W	—
$R_{th,c,h}(4)$	0.88×10^{-3} K/W	—
$R_{th,c,h}(5)$	0.14×10^{-3} K/W	—
$C_{th,c,h}(1)$	337.28 Ws/K	—
$C_{th,c,h}(2)$	409.76Ws/K	—
$C_{th,c,h}(3)$	1.37×10^3 Ws/K	—
$C_{h,c,h}(4)$	1.91×10^4 Ws/K	—
$C_{h,c,h}(5)$	1.30×10^4 Ws/K	—
TC_{Esw}	0.003	[30]
TC_{Err}	0.006	[30]
T_{ref}	125°C	—